

Spectral ratios for the Pembina Cardium formation computed with virtual sources

Arnim B. Haase, Donald C. Lawton and Abdullah A. Alshuhail

ABSTRACT

Spectral ratios across the Pembina-Cardium formation are computed from surface source lines and down-hole receiver gathers by applying virtual source principles. It is found necessary to apply first-arrival wave package windowing to reduce ringing of these spectral ratios. There is an increase of attenuation across the reservoir layer for all three source line experiments following CO₂ injection. This attenuation increase is confirmed by spherical wave modelling employing a multi-interface Sommerfeld integral algorithm and using monitor well-logs as well as fluid substitution derived perturbations of reservoir parameters. Spherical wave modelling also shows far-offset tuning across the reservoir when offsets are retained rather than applying virtual source methods. Alternate measures of CO₂ injection effects are demonstrated by displaying time domain maximum amplitude differences as function of offset as well as plotting frequency domain magnitude spectral differences as function of frequency and offset.

INTRODUCTION

The Violet Grove CO₂ seismic monitoring project is described by Lawton et al. in a 2005 CREWES Report. Both, a baseline survey and a first monitor survey, were acquired in March and December 2005, respectively. This data has been analyzed by F. Chen (2006) [surface data analysis], M. Coueslan (2007) [VSP data analysis] and one of the authors (A. Alshuhail) as part of their Thesis work. The impetus to the work reported here comes from one of the authors (D. Lawton) who suggested utilizing virtual-source-method derived spectral ratios across the Cardium formation to shed further light on the CO₂-monitoring question. Well-log based spherical wave modeling incorporating fluid-substitution derived rock property variations (F. Chen, 2006) is employed to check real-data spectral ratios and to introduce maximum amplitude spectral difference measurements.

REVIEW OF VIRTUAL SOURCES

An excellent description of virtual source principles can be found in a Leading Edge contribution by Bakulin et al. (2007). Their depiction of the method is repeated in our Figure 1. In their words:

... it suffices to visualize the technique as a cross-correlation of direct-arrival energy at one buried geophone (the virtual source) with the trace recorded at a second geophone (the receiver). The result, once summed over a suitable set of illuminating physical sources, approximates the response of a buried source-receiver pair in the subsurface. This data-driven virtual source re-datuming process does not require any velocity information.

The purpose of this exercise is to image below complex and/or time-varying overburden in general and, in our particular application, we hope to improve the repeatability of our

time-lapse surveys by eliminating surface variability. Bakulin et al. (2007) also point out that, in theory, for correct results physical sources should completely surround the area of interest and that, in practice, because of limited apertures dictated by surface sources we introduce artifacts and unwanted arrivals. We are aiming for a relative comparison of spectral ratios and as long as the “side-effects” are comparable no error contributions are expected, an assumption that must be tested eventually. The equation given in Figure 1 represents a time-domain approach. Because we require spectra for spectral ratios all input traces are Fourier-transformed and time-domain cross-correlations are replaced by complex conjugate multiplications in the frequency domain.

INVESTIGATING THE SPECTRA OF PEMBINA-CARDIUM VIRTUAL SOURCES

A map view of shot locations, 2D receiver line lay-out and the monitor well location are given in Figure 2 (Coueslan, 2007, Figure 1.7). Because of issues with non-repeated shots between the baseline survey and the monitor survey (Coueslan, 2007) we initially concentrate on line 3 shot locations. In addition to the surface line receivers, every shot is also recorded by 7 down-hole receivers in the monitor well. For line 3 there are 63 surface shots, and the corresponding vertical component down-hole receiver gathers are plotted in Figure 3. The left-most 63 traces are recorded at the deepest receiver (1640m depth) and the adjacent group of 63 traces at the receiver just above (1620m depth); these two receivers bracket the Cardium Reservoir. First arrival times are earlier for shot locations that are closer to the monitor well and also earlier for shallower receivers, as expected. Baseline magnitude spectra for top- and bottom-reservoir, obtained by virtual source method application, are displayed in Figure 4. On the right side of Figure 4 the signal disappears under the noise floor and from the characteristic look of both spectra around 60Hz it is concluded that a 60Hz notch-filter is deployed. The monitor survey equivalent to Figure 4 is shown in Figure 5. One very noticeable change is the 180Hz spike in Figure 5; this is the third harmonic of a 60Hz power grid/power generator and suggests equipment changes. Spectral ratios are computed by taking the ratio of magnitude values, one frequency point at a time. The ratios derived from the magnitude spectra in Figures 4 and 5 for frequencies below 60Hz are given in Figure 6; the two curves are aligned at the left margin to highlight departure with increasing frequencies. There is a discernable trend but it is difficult to see because of the ringing in the spectral ratios.

All spectra and their ratios computed thus far are derived from the input traces without any windowing applied. Multiplying input traces with a fairly narrow Gaussian window ($\exp[-30t^2]$) to attenuate reflections and noise beyond the first-arrival wave-package leads to the windowed traces in Figure 7 and the much smoother magnitude spectra in Figures 8 and 9. Both recomputed spectral ratios given in Figure 10 are much smoother as well when compared to their equivalent before trace windowing (Figure 6); the curves of Figure 10 are aligned at the left margin also. Figure 10 demonstrates a change of spectral ratio slope following CO₂ injection in the frequency range below the 60Hz notch: there is more attenuation across the reservoir-interval. All 63 sources of line 3 are included in the virtual source computations presented above. What is the sensitivity of spectral ratios with respect to offset range changes? This question is answered with monitor line restricted offset range spectral ratios presented in Figure 11; compared are far-offsets,

mid-offsets and near-offsets as input to virtual source computations. Above about 15Hz there are frequency bands of significant offset-dependent variations in spectral ratios.

Offset distribution differences between source lines 1, 2 and 3 can be gleaned from Figure 2. Because of these offset differences some variation in the general shape of spectral ratios are to be expected for lines 1 and 2; but is the presumed CO₂ driven increase in attenuation across the reservoir interval, observed for line 3, also noticeable for lines 1 and 2? The answer from Figures 12 and 13 is affirmative; there is an attenuation increase for lines 1 and 2 similar to line 3. What is more, the general spectral ratio shape is closest between the two lines that are parallel and have similar minimum offsets (lines 2 and 3). That all three lines point to a reservoir–attenuation increase for the monitor survey boosts our confidence that CO₂ injection might be the cause. A modelling study could bring further confirmation and that approach is taken in the next section.

MODELLING SPECTRAL RATIOS WITH A PEMBINA WELL LOG

The modelling algorithm employed for this study is based on a multi-interface Sommerfeld integral (Haase, 2008) that computes a 3D wave-field for a 1D earth-model. The resulting elastic/anelastic wave-field is composed of a near-field as well as a far-field and models spherical spreading for vertically inhomogeneous media. The required 1D earth-model is derived from a well-log of the observation well. Velocity spikes at the top and at the bottom of the log are edited. A velocity ramp is chosen for the shallow section above the log to, firstly, ensure a correct overburden travel time and to, secondly, prevent a nonzero reflection coefficient at the top of the log. Figure 14 shows the corrected log that is input to the Sommerfeld modelling algorithm. An offset distribution is computed with the same start- and end-point as shot line 3 and 63 equidistant shot locations. This is not exactly the same shot location distribution as line 3 in Figure 2, a point which needs to be tested later. For baseline modelling the above information is sufficient. Monitor line modelling requires modification of reservoir parameters with Gassmann fluid substitution derived perturbations. Chen (2006) reports values of

$$\Delta\rho = -2.5\% ,$$

$$\Delta V_p = -4.62\% \text{ and}$$

$$\Delta V_s = +1.19\%$$

for 90% CO₂ saturated Pembina Cardium sand, and those reservoir parameter perturbations will be adopted here too.

Restricted offset-range spectral ratios resulting from baseline model computations are plotted in Figure 15. There are similarities in general curve shape and offset dependence when compared to the real data equivalent given in Figure 11, but why is there no closer agreement? Unequal shot location distribution between model and data could be one possible explanation and requires further investigation. Once the model traces for baseline and monitor survey are computed, the procedure for obtaining spectral ratios is equivalent to the real data situation. Model derived spectral ratios can be seen in Figure 16. As is done for spectral ratio displays above, the curves of Figure 16 are aligned at the left margin. These spectral ratios show an increase in attenuation across the reservoir

layer when 90% CO₂ saturation is modelled which increases our confidence in the results obtained from baseline and monitor data (Figures 10, 12 and 13).

MODELLING SPECTRAL DIFFERENCES WITH A PEMBINA WELL LOG

Application of the virtual source method allows the reduction of surface variability effects, but the price paid is the loss of the offset dimension. What, if anything, could be gained from including offset in our analysis? With the same parameters as used above for spectral ratio modeling, offset dependent traces are computed for receivers placed on top and the bottom of the baseline reservoir layer; transmitted wave vertical components are displayed in Figure 17, where top-of-reservoir signals are given in red and bottom-of-reservoir signals are shown in black. Even at this plotting scale curiosity is awakened by the far-offset trace in Figure 17, which is re-plotted at a larger scale in Figure 18. It comes as no surprise that travel time to bottom-of-reservoir exceeds travel time to the reservoir top, but the amplitude increase requires an explanation. The displayed transmitted-wave-vertical-component is only part of the computed total wave-field; in conjunction with the reflected wave-field, layer reverberations can be set up that could lead to far-offset tuning. Tuning is a good thin-layer indicator and is expected to be sensitive to parameter changes due to CO₂ injection. Differences between the maximum amplitude values of top-of-reservoir traces and bottom-of-reservoir traces are shown in Figure 19. Clearly, beyond approximately 900m offset, the bottom-of-reservoir signal is stronger, which leads to a polarity change of the difference curve and indicates offset tuning. The jitter of the difference curve is typical for maximum amplitudes picked from discretized data and can be reduced by finer sample intervals, as is done for Figure 20. In addition to the smoothed baseline model difference curve, Figure 20 also displays a monitor model difference curve, which is at or mostly above (more positive) the baseline equivalent everywhere, and curve separation increases with offset. The explanation for the more positive values of the monitor model differences lies in the fact that reservoir bottom signals are more attenuated, and therefore smaller numbers are subtracted to form the monitor model differences when compared to baseline model differences.

When, instead of time-domain amplitude maxima $a(t)_{max}$, the magnitudes of frequency components $|A(\omega)|$ are used, we introduce frequency as an additional variable and compute spectral differences as functions of frequency and offset. Figure 21 shows the difference between the monitor model spectrum and the baseline model spectrum at the reservoir bottom, which is the difference of baseline model spectra (top minus bottom) minus the difference of monitor model spectra (top minus bottom). Without CO₂ injection Figure 21 would show a horizontal plane. Noise reduction could be achieved by partial offset stacking and frequency smoothing before computing Figure 21 or by averaging between neighboring points in Figure 21. It would be interesting to calibrate this procedure with theoretical CO₂ saturations and then compare it to actual data spectral differences.

CONCLUSIONS

The virtual source method described by Bakulin et al. (2007) is employed to derive virtual source/receiver pairs at top and bottom of the Pembina-Cardium formation and to compute spectral ratios across the reservoir layer. Considerable ringing in these ratios is reduced by applying a tight Gaussian window to the input traces. An increase in

attenuation across the reservoir layer following CO₂ injection is noted in all three source line experiments. When introducing CO₂ injection driven reservoir parameter perturbations, as derived by F. Chen (2006) from Gassmann's fluid substitution equations, into spherical wave modeling with monitor well information we notice a similar reservoir layer attenuation increase.

The price paid for applying virtual source methods is the loss of offset information. Offset-related tuning across the reservoir layer is noted following offset dependent modelling with a multi-interface Sommerfeld integral and displaying time domain maximum amplitude differences. Spectral magnitude differences can also be displayed as function of frequency and offset to further highlight the effects of CO₂ injection.

ACKNOWLEDGEMENTS

Support from the CREWES Project at the University of Calgary and its industrial sponsorship is gratefully acknowledged.

REFERENCES

- Bakulin, A., Mateeva, A., Mehta, K., Jorgensen, P., Ferrandis, J., Sinha Herhold, I., and Lopez, J., 2007, Virtual source applications to imaging and reservoir monitoring: *The Leading Edge*, **26**, 732-740.
- Chen, F., 2006, Interpretation of time-lapse surface seismic data at a CO₂ injection site, Violet Grove, Alberta: M.Sc. Thesis, University of Calgary.
- Coueslan, M.L., 2007, Processing and interpretation of time-lapse Vertical Seismic Profile data from the Penn West CO₂ monitoring project: M.Sc. Thesis, University of Calgary.
- Haase, A.B., 2008, Extending Sommerfeld integral based spherical wave field computations beyond two layers: CREWES Research Report, Volume 20.
- Lawton, D., Coueslan, M., Chen, F., Bland, H., Jones, M., Gallant, E., and Bertram, M., 2005, Overview of the Violet Grove CO₂ seismic monitoring project: CREWES Research Report, Volume 17.

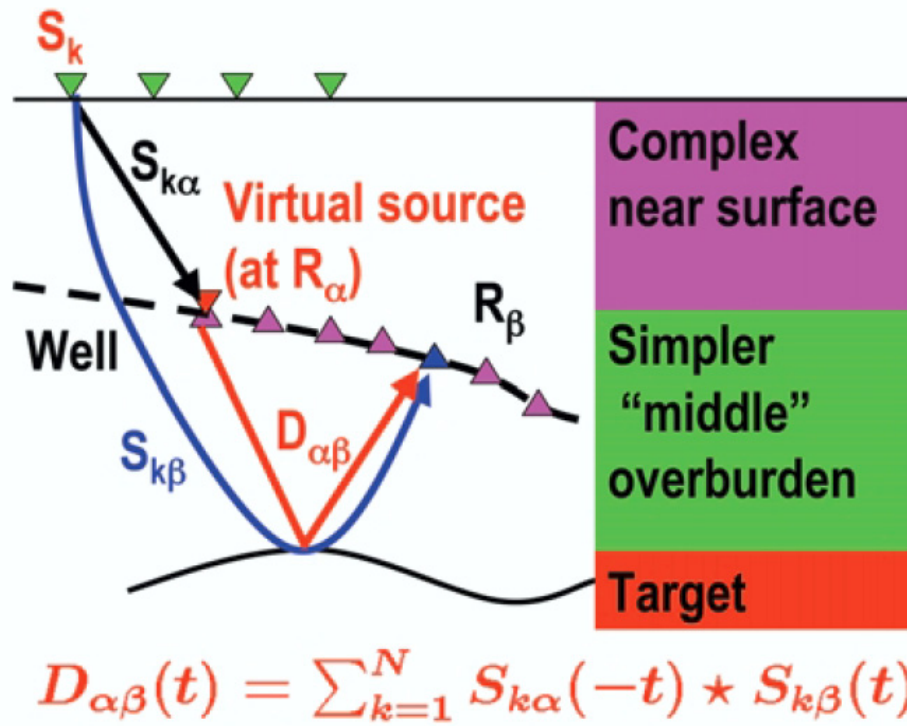


FIG.1. Schematic of virtual source method (Bakulin et al., June 2007, The Leading Edge).

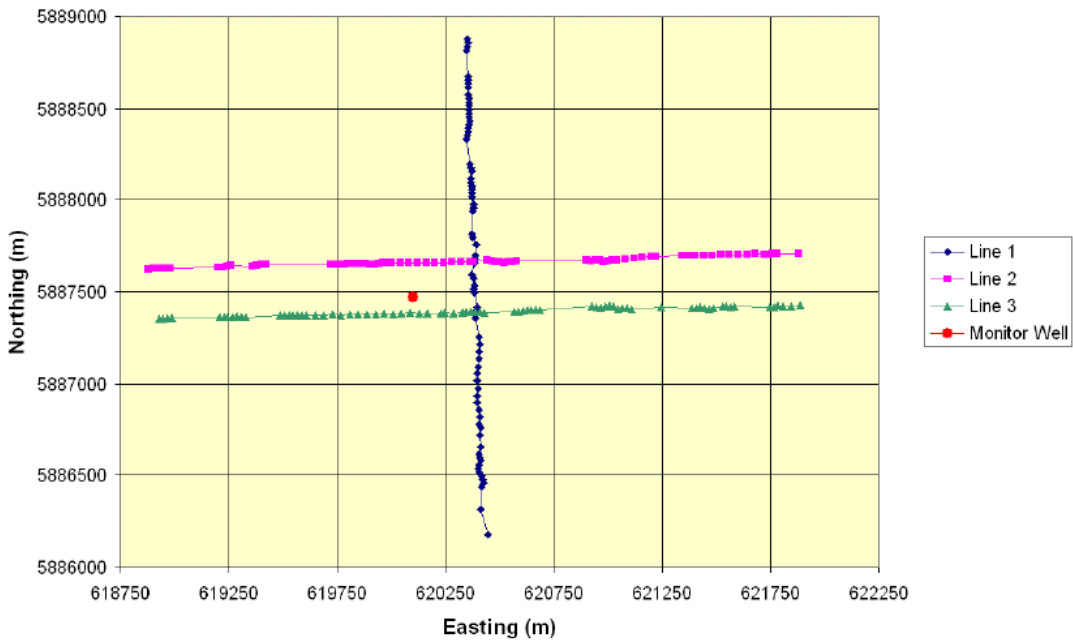


FIG.2. Shot locations for the baseline survey (Coeslan, 2007, Fig. 1.7).

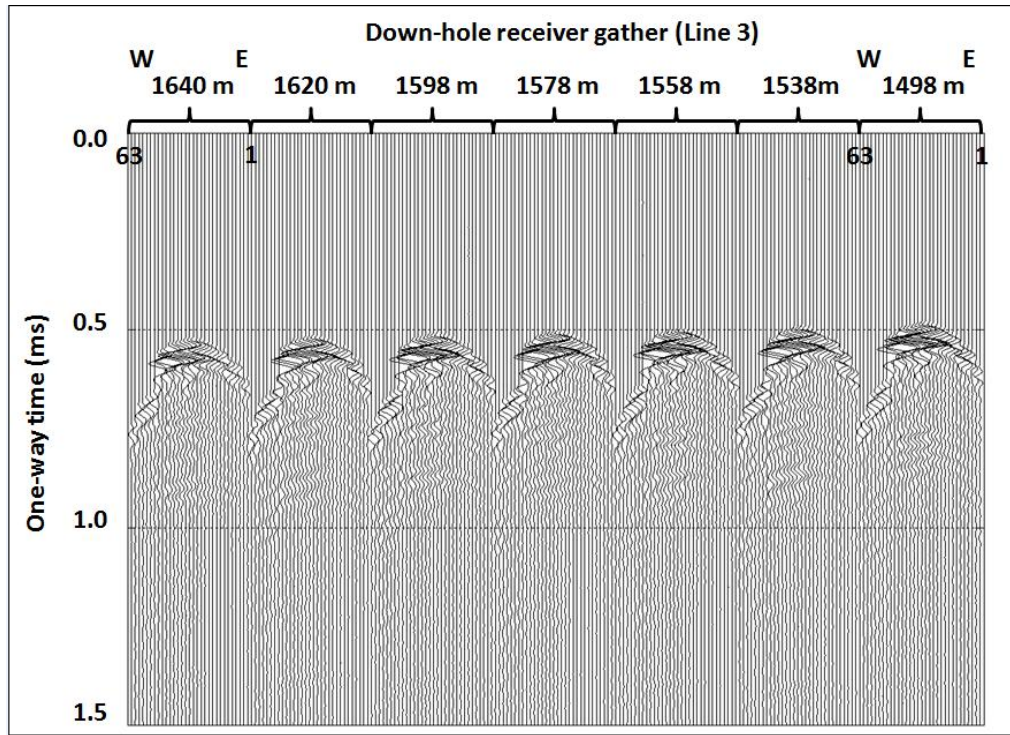


FIG.3. Down-hole receiver gathers for line 3 (vertical components).

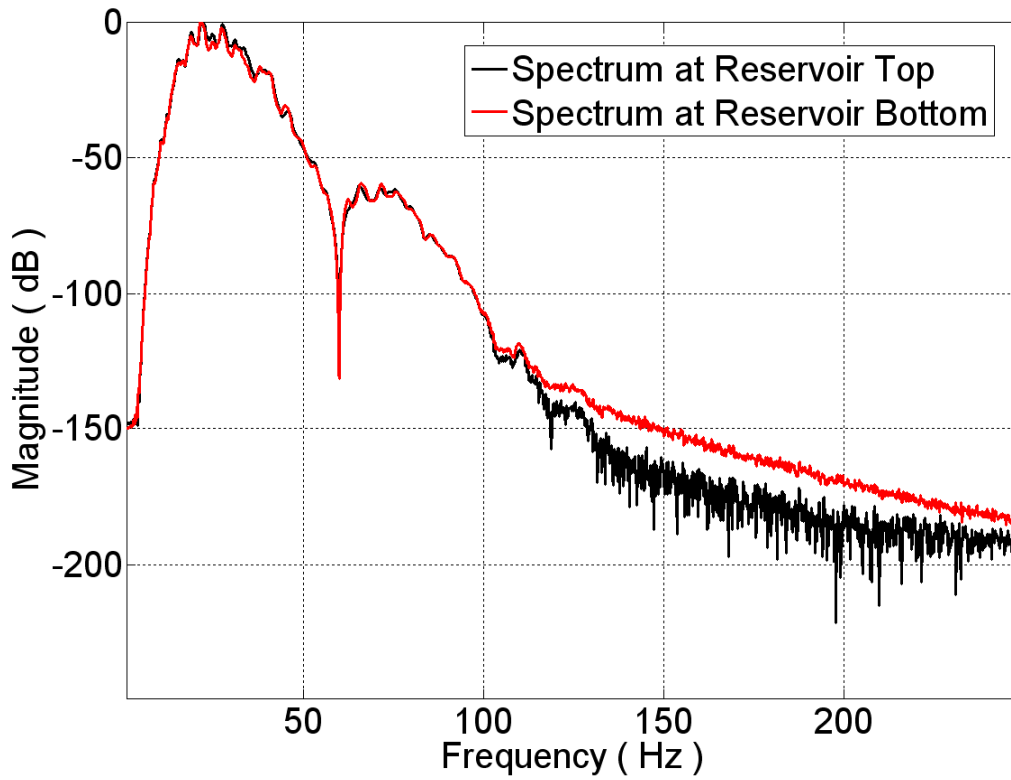


FIG.4. Base line VSP-trace interferometry spectrum

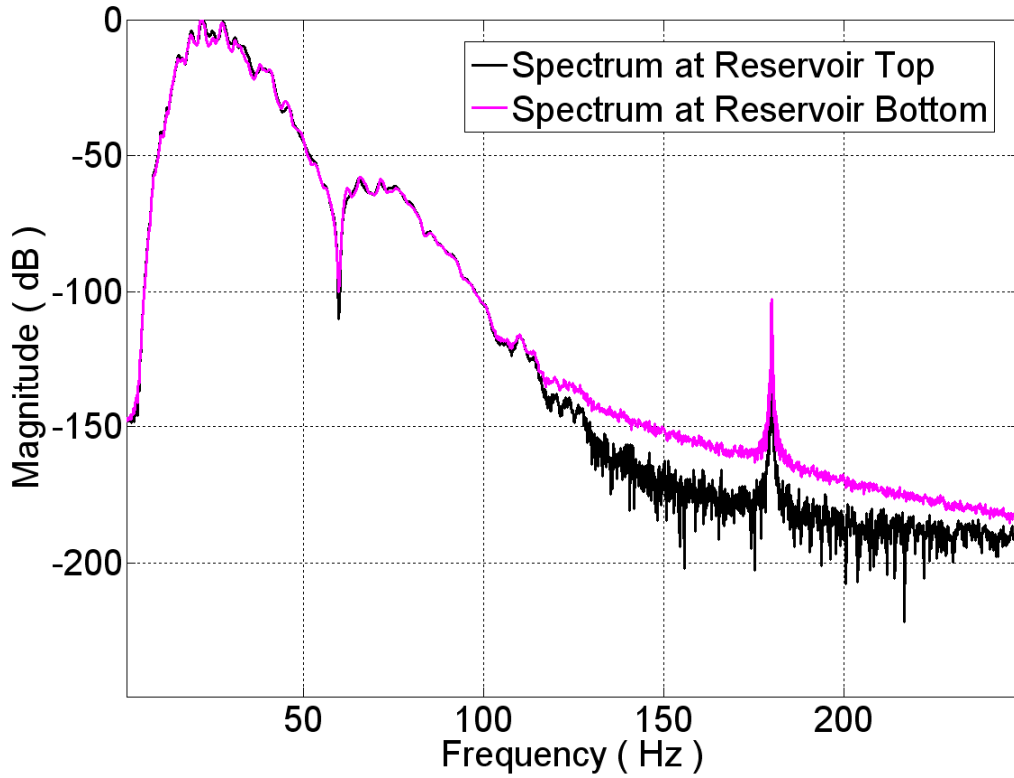


FIG.5. Monitor line VSP-trace interferometry spectrum.

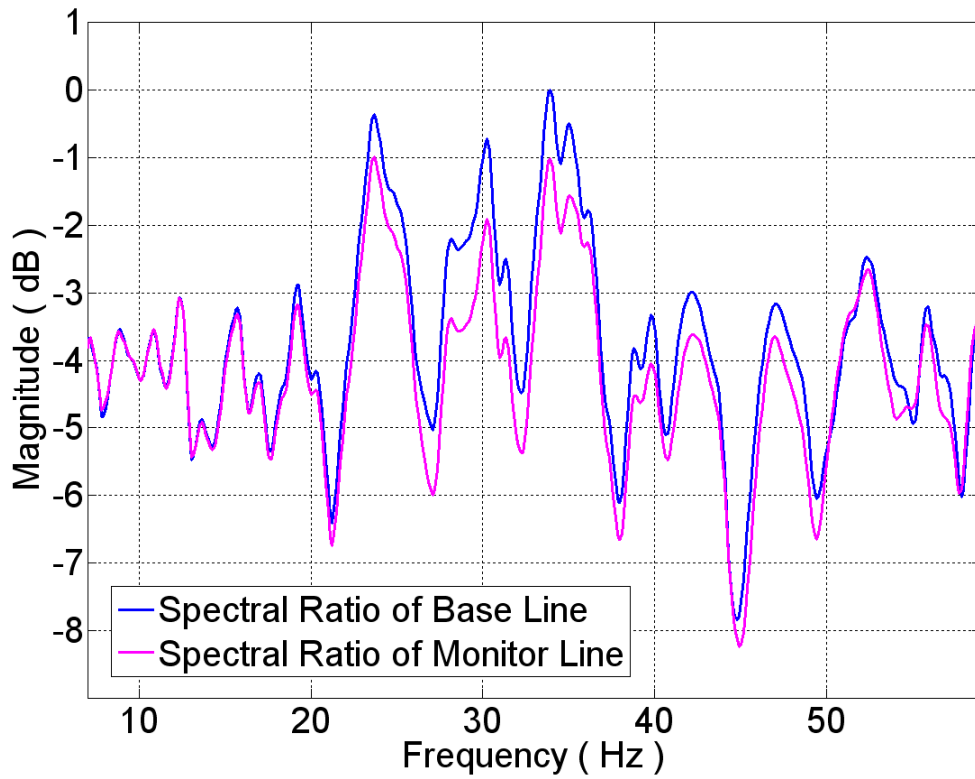


FIG.6. VSP-trace interferometry spectral ratios.

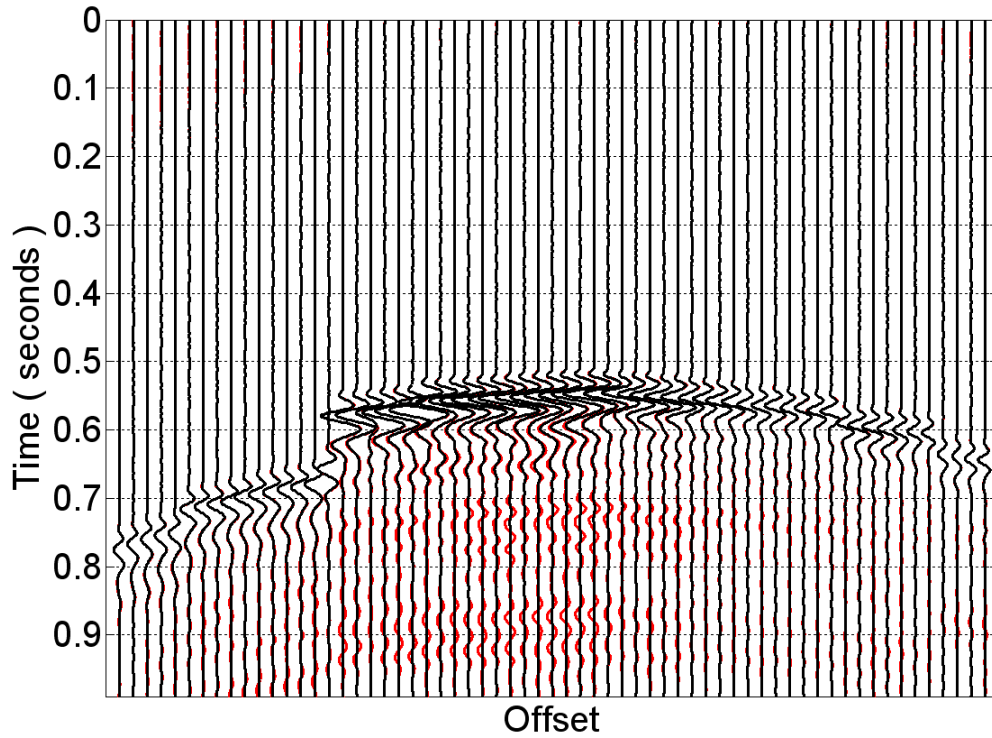


FIG.7. VSP-traces before (red) and following (black) Gaussian windowing of first arrival.

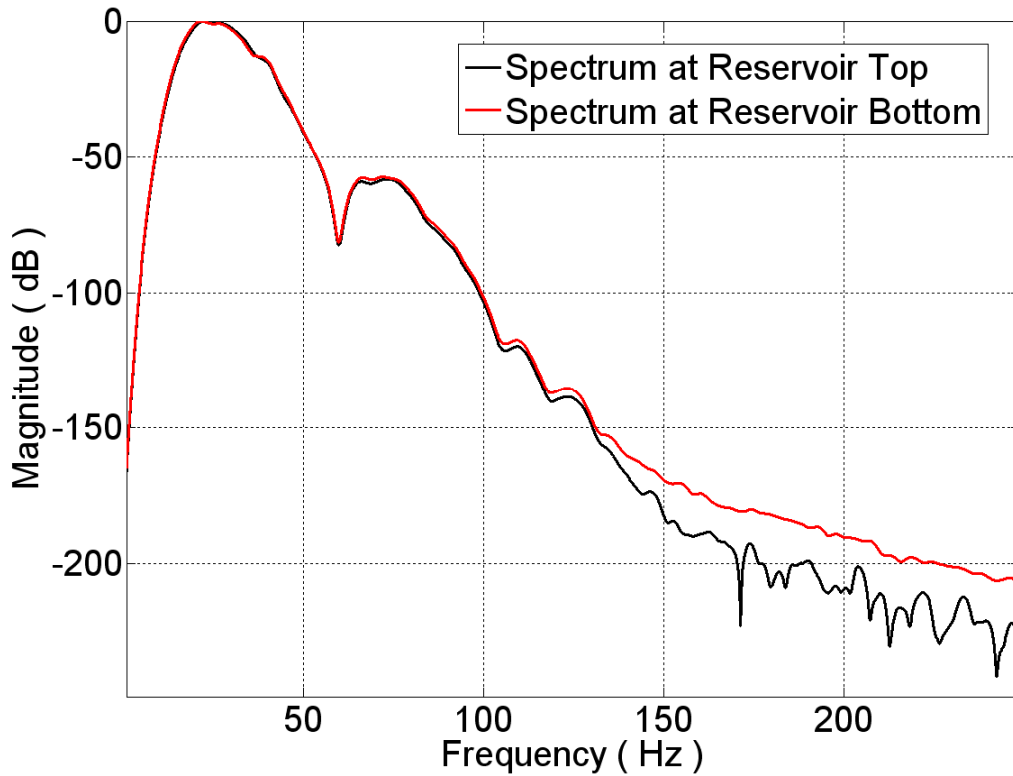


FIG.8. Base line VSP-trace interferometry spectrum (Gaussian window applied).

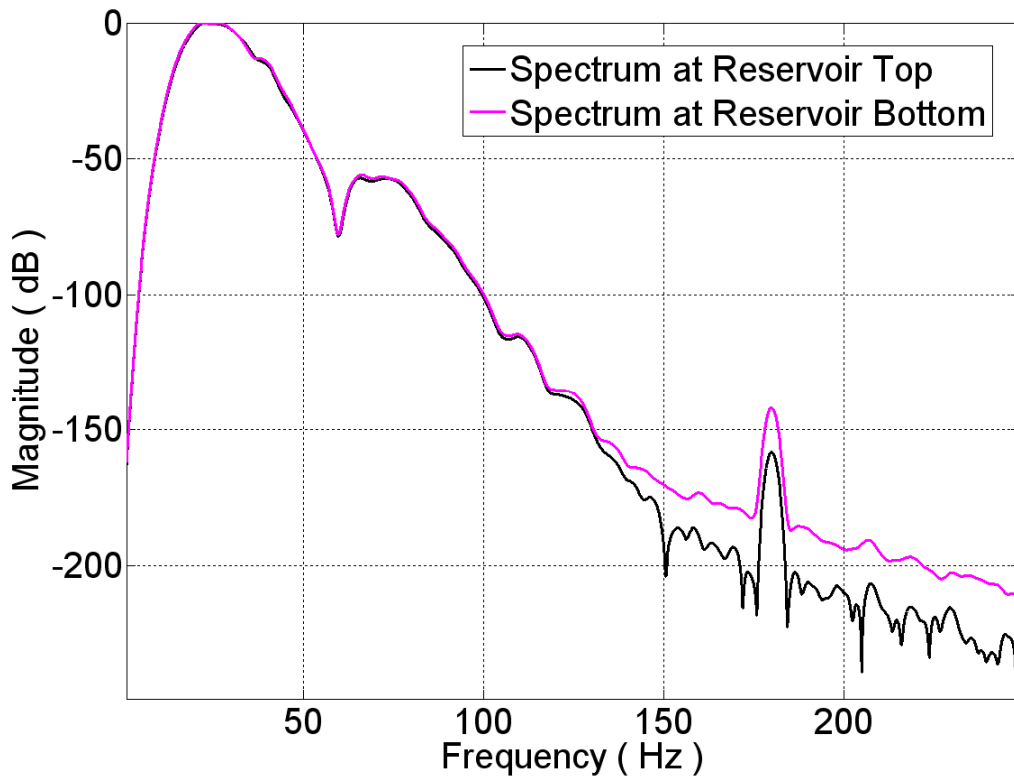


FIG.9. Monitor line VSP-trace interferometry spectrum (Gaussian window applied).

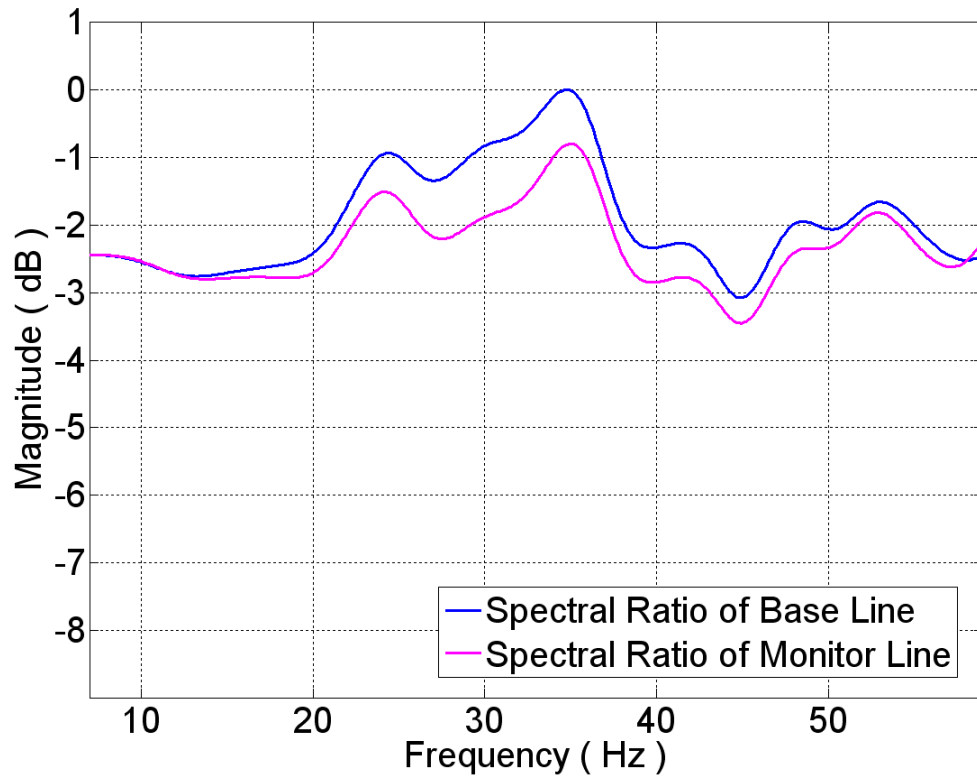


FIG.10. VSP-trace interferometry spectral ratios of line 3 (Gaussian window applied).

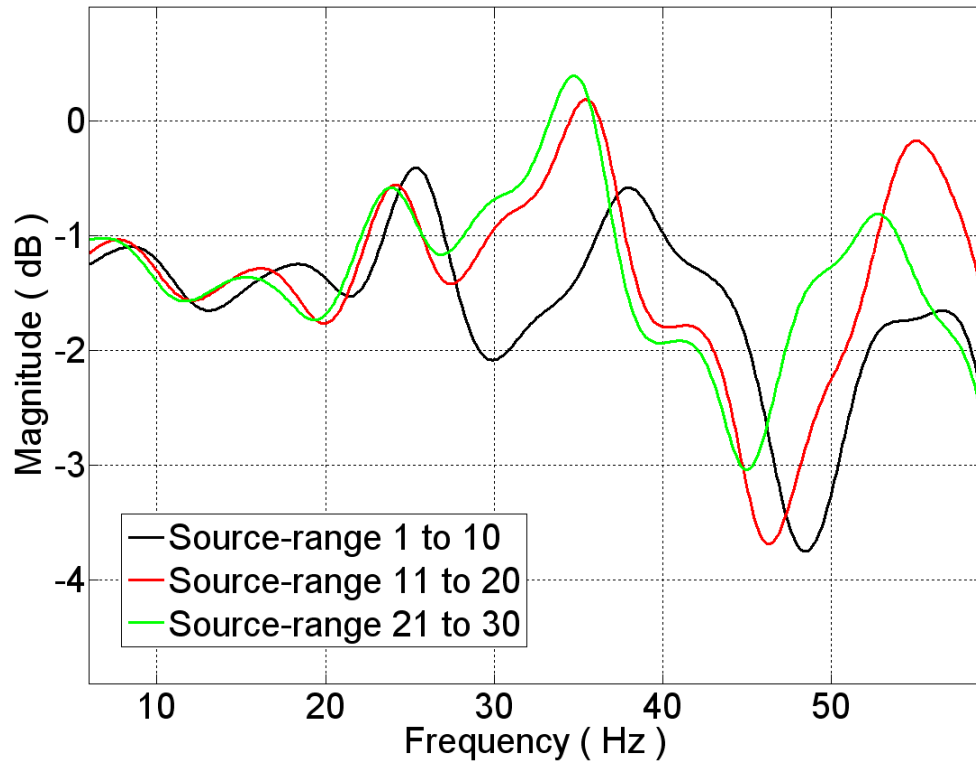


FIG.11. Source range dependence of monitor line VSP-trace interferometry spectra.

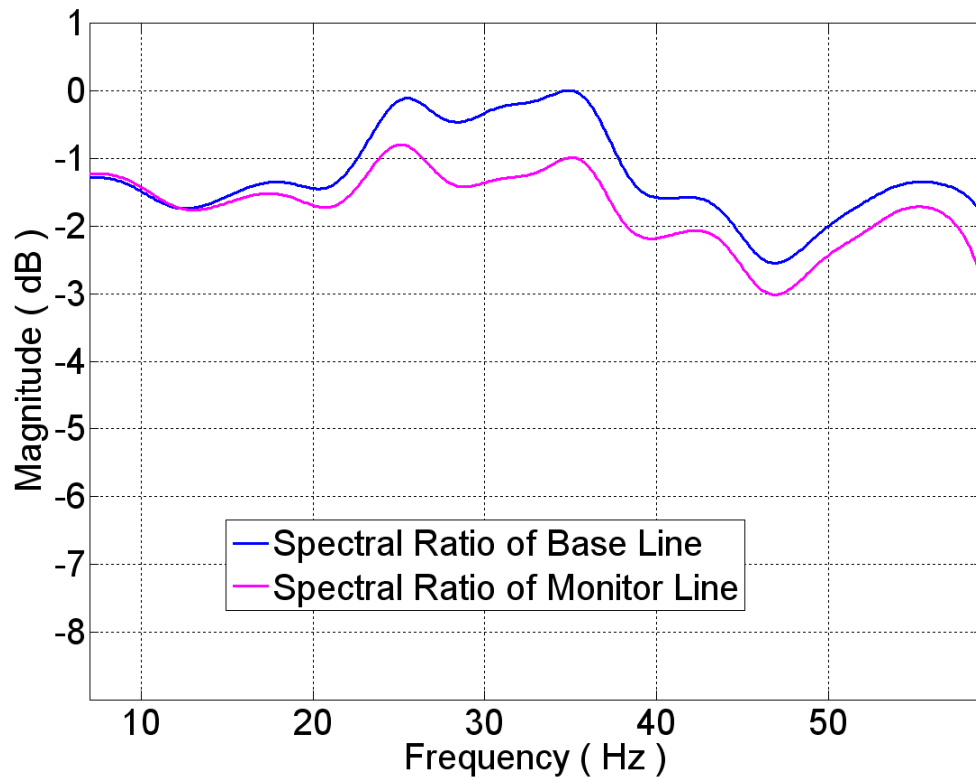


FIG.12. VSP-trace interferometry spectral ratios of line 1 (Gaussian window applied).

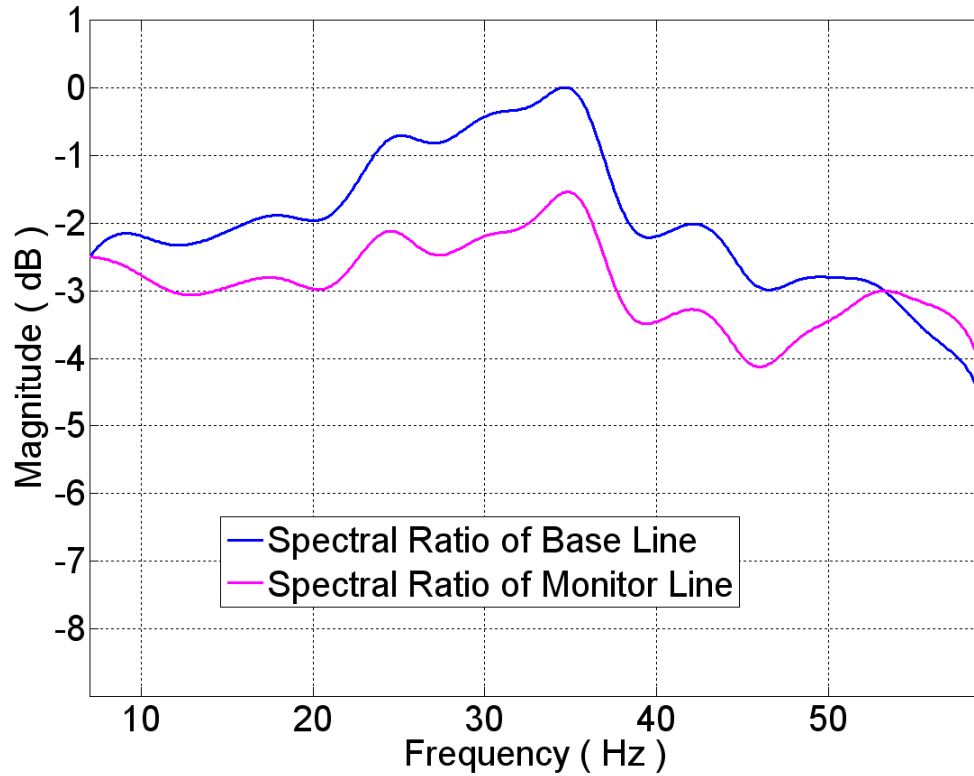


FIG.13. VSP-trace interferometry spectral ratios of line 2 (Gaussian window applied).

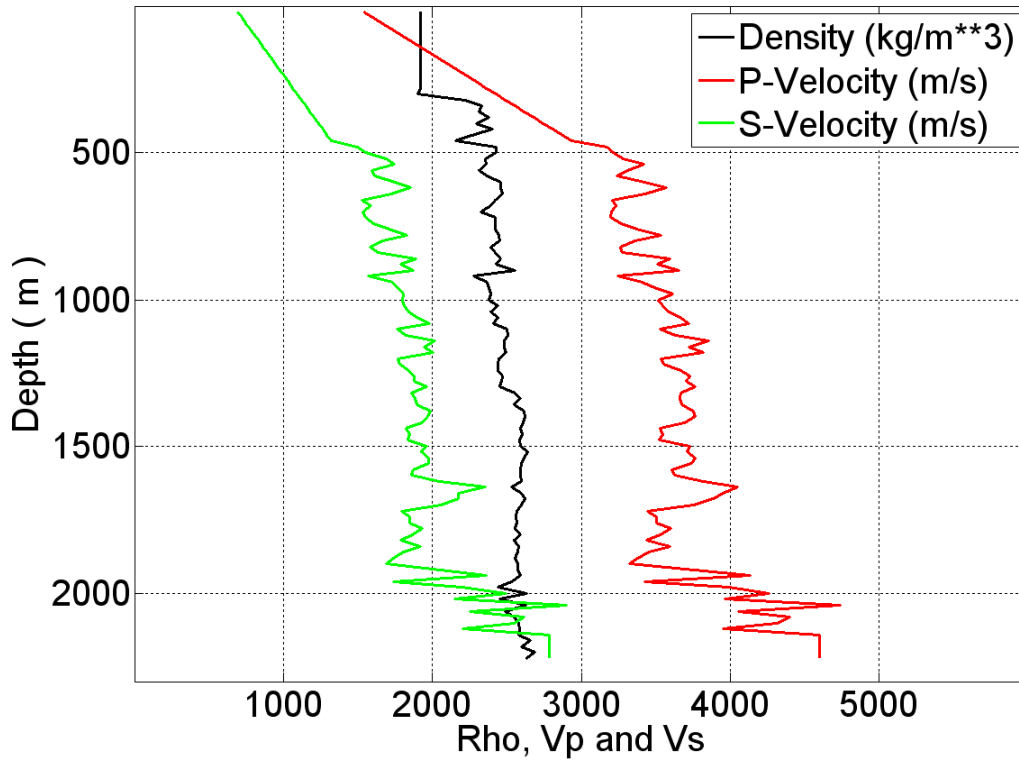


FIG.14. Edited Pembina log velocities and density.

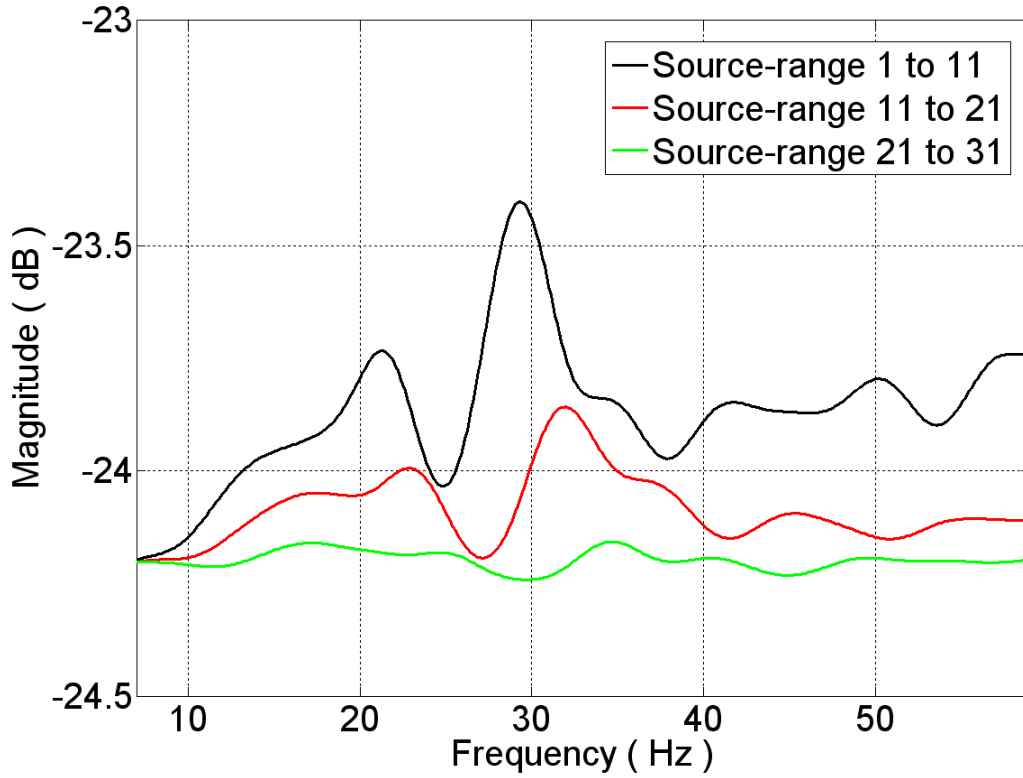


FIG.15. Source range dependence of VSP-model interferometry spectral ratios.

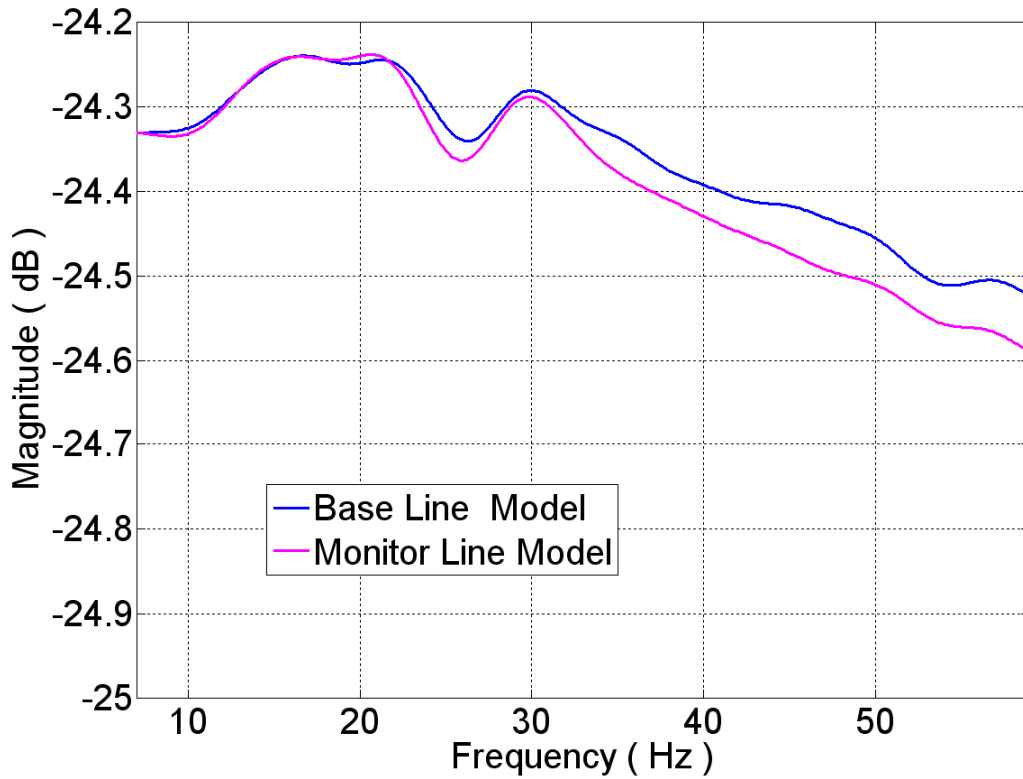


FIG.16. VSP-model interferometry spectral ratios.

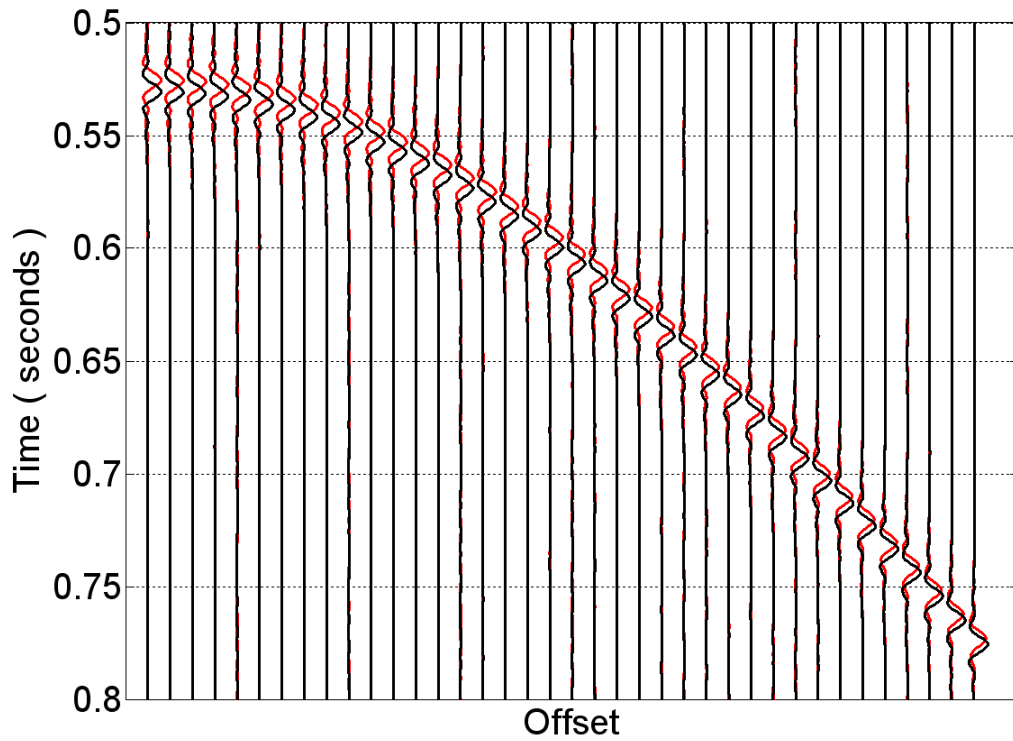


FIG.17. Model transmitted wave vertical components (red at reservoir top and black at bottom).

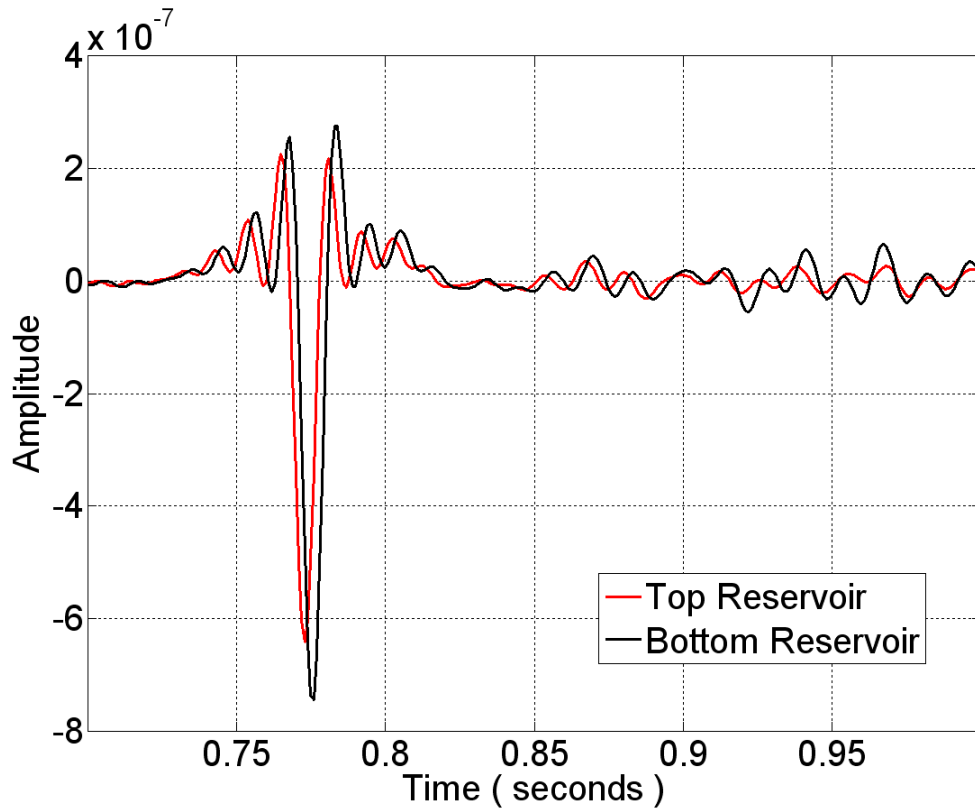


FIG.18. Model transmitted wave vertical components at far offset.

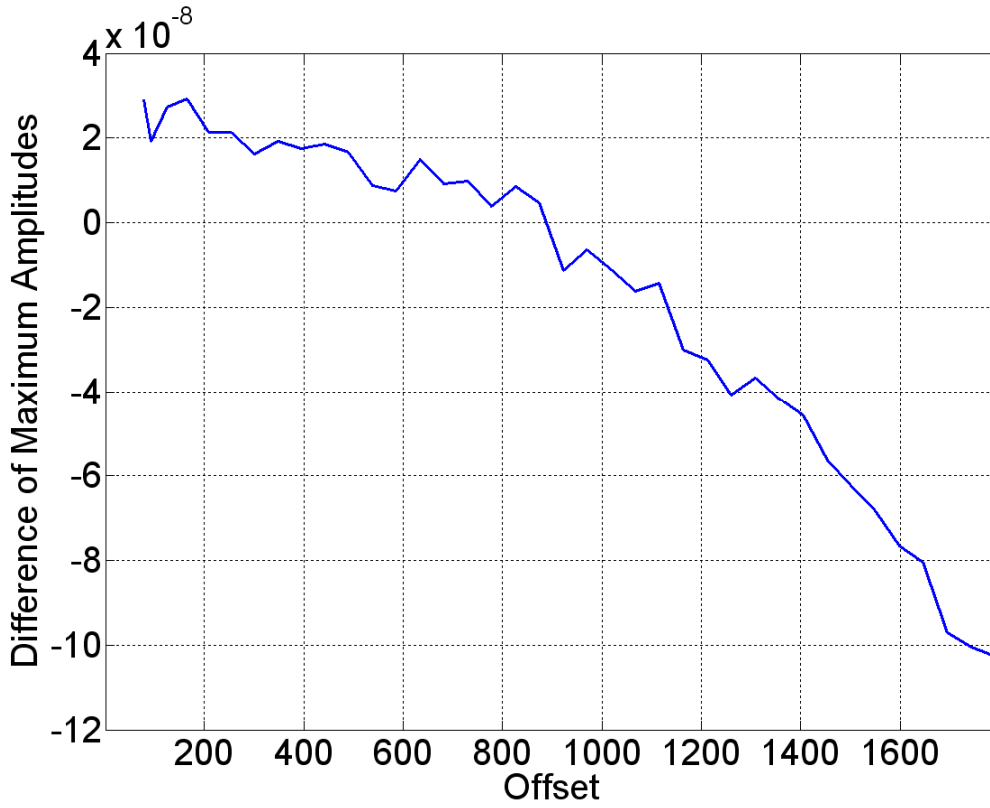


FIG.19. Maximum amplitude differences of baseline model.

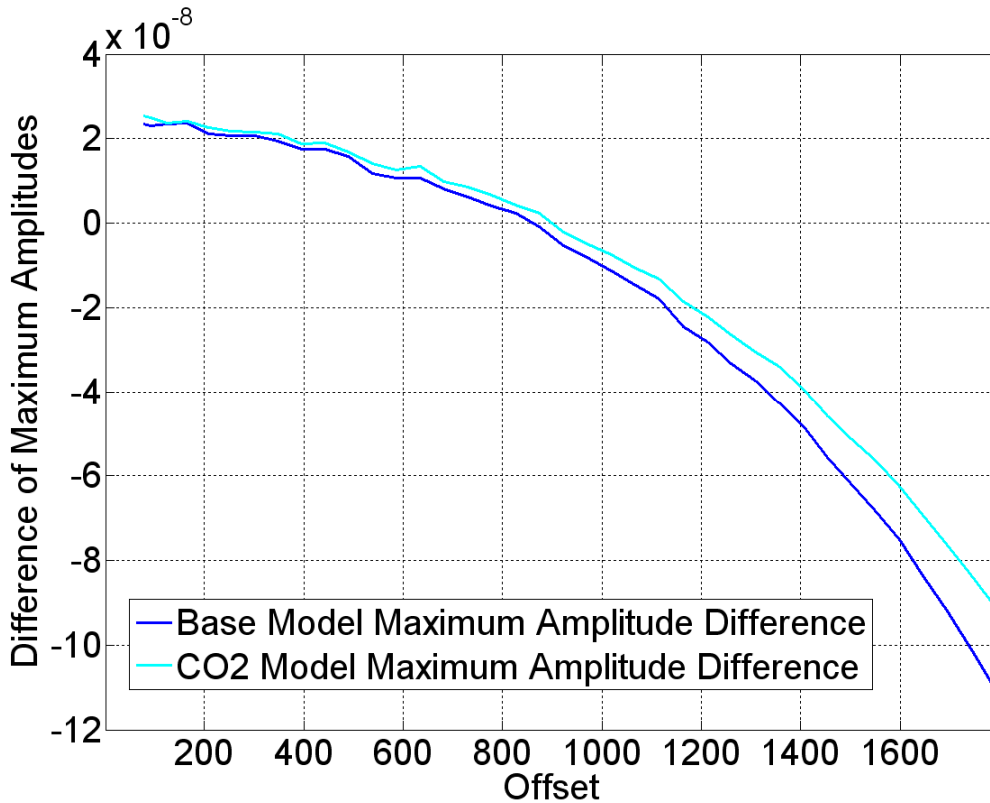


FIG.20. Smoothed maximum amplitude differences of both models.

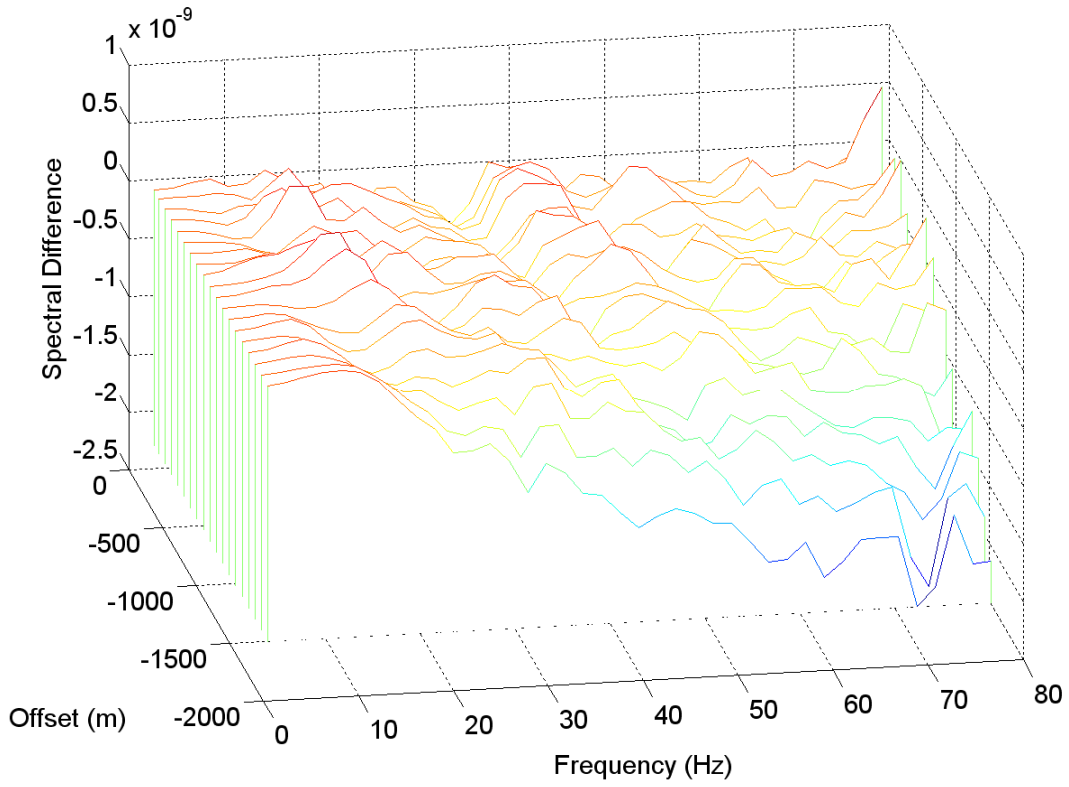


FIG.21. Baseline-model to CO2-model differences as function of offset and frequency.